Supporting Information

Tunable Luminescent Lanthanide Cluster-Based Hydrogel Probe for Ratiometric Detection of Ofloxacin, Anti-Counterfeiting, and Magnetocaloric Applications

Tiantian Wang, Hao Wang and Wenbin Sun*[a]

[a] Key Laboratory of Functional Inorganic Material Chemistry Ministry of Education, School of Chemistry and Material Science Heilongjiang University, 74 Xuefu Road, Harbin 150080, P. R. China. *E-mail: wenbinsun@126.com*

Table S1 Crystallographic data for **Gd_{14}**.

	Gd_{14}
Empirical formula	$C_{126}H_{200}Gd_{14}O_{66}$
Formula weight	4972.35
Crystal system	tetragonal
Space group	I4/mmm
Temperature (K)	273.15
a (Å)	21.2689(14)
b (Å)	21.2689(14)
c (Å)	21.2497(15)
α (°)	90
β (°)	90
γ (°)	90
V (Å^3)	9612.6(14)
ρ_{calc} (Mg m^{-3})	1.718
μ (mm^{-1})	4.825
F(000)	4760.0
Collected reflections	29580
Independent reflections	2167
*R*int	0.0609
R_1 [$I > 2\sigma(I)$]	0.0442
wR_2 (all data)	0.0984
Goodness of fit on F^2	1.104
CCDC number	2403575

Table S2 Selected bond lengths (Å) for **Gd_{14}**.

Gd1-O2^{1}	2.455(8)	Gd3-O6	2.465(6)
Gd1-O2^{2}	2.455(8)	Gd3-O7	2.329(8)
Gd1-O2	2.455(8)	Gd3-O8	2.339(10)
Gd1-O2^{3}	2.455(8)	Gd2-O1^{5}	2.6509(11)
Gd1-O1A	2.401(8)	Gd2-O1	2.6510(11)
Gd1-O1^{3}	2.64203(18)	Gd3-Gd3^{3}	3.6096(11)
Gd1-O1	2.64200(18)	Gd3-O2^{3}	2.317(5)
Gd1-O1^{2}	2.64203(18)	Gd3-O2	2.317(5)
Gd1-O1^{1}	2.64203(18)	Gd2-O1A	2.423(4)
Gd2-O3	2.354(10)	Gd2-O4	2.417(8)

Table S3 Selected bond angles (°) for **Gd_{14}**.

O2^{1}-Gd1-O2^{2}	72.10(18)	O1A^{1}-Gd2-O1^{5}	118.68(19)
O2^{1}-Gd1-O2^{3}	112.7(4)	O1A^{1}-Gd2-O1^{6}	75.24(15)
O2^{3}-Gd1-O2	72.10(18)	O1^{6}-Gd2-O1	130.26(7)
O2-Gd1-O1^{2}	139.73(2)	O1^{1}-Gd2-O1	80.17(2)
O2^{1}-Gd1-O1^{3}	139.73(2)	O1^{5}-Gd2-O1	79.45(6)
O2^{1}-Gd1-O1^{1}	71.79(14)	O2^{3}-Gd3-O2	77.2(4)
O2^{2}-Gd1-O1^{3}	71.79(14)	O2-Gd3-O5	66.7(3)
O2^{3}-Gd1-O1^{2}	139.726(19)	O2^{3}-Gd3-O5	66.7(3)
O1A^{1}-Gd1-O2^{1}	80.9(2)	O2^{3}-Gd3-O6	130.5(3)
O1A^{1}-Gd1-O2^{2}	143.23(6)	O2-Gd3-O6	78.7(2)
O1A^{2}-Gd1-O2^{1}	80.9(2)	O2-Gd3-O6^{3}	130.5(3)
O1A^{3}-Gd1-O2^{2}	80.9(2)	O2-Gd3-O7	98.6(3)
O1A^{3}-Gd1-O2^{3}	80.9(2)	O2-Gd3-O7^{7}	155.4(3)
O1A^{2}-Gd1-O2^{3}	143.23(6)	O2-Gd3-O8	79.7(2)
O1A^{3}-Gd1-O^{2}	143.23(6)	O5-Gd3-Gd^{1}	54.8(4)
O1A^{2}-Gd1-O2^{2}	80.9(2)	O5-Gd3-Gd3^{1}	45.46(5)
O1A-Gd1-O2	80.9(2)	O6-Gd3-Gd1	103.48(15)
O1A^{1}-Gd1-O1A	70.31(18)	O6-Gd3-Gd3^{1}	42.94(14)
O1A2-Gd1-O1A	109.0(4)	O6-Gd3-O5	64.2(3)
O3-Gd2-O1^{1}	138.56(8)	O6^{3}-Gd3-O6	85.3(5)
O4-Gd2-O4^{5}	126.9(4)	O7B-Gd3-Gd1	135.1(2)

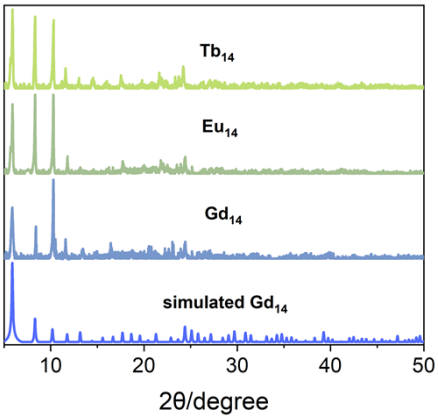

Fig. S1 Experimental and simulated PXRD patterns of **Ln_{14}**.

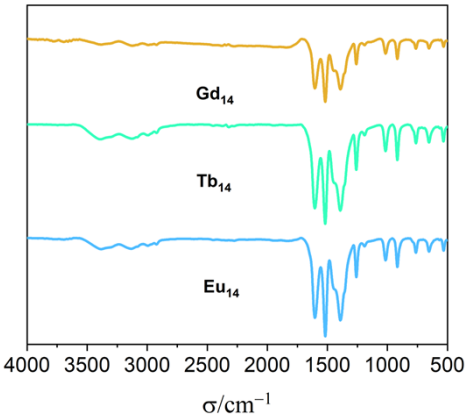

Fig. S2 Infrared spectra of **Ln_{14}**.

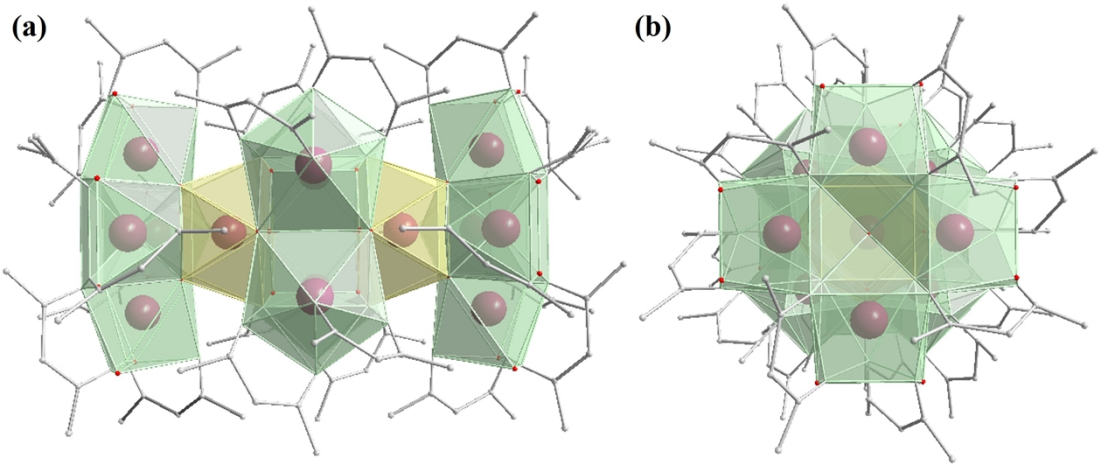

Fig. S3 Polyhedral view of the structure along the crystallographic a-axis (a) and c-axis (b) of **Gd_{14}**. Color code: Gd (plum), O (red), C (grey). H atoms were omitted for clarity.

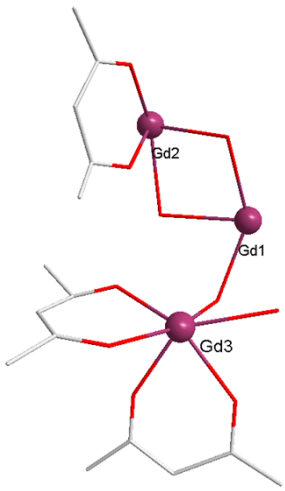

Fig. S4 Asymmetric unit of **Gd_{14}**. Color code: Gd (plum), O (red), C (grey). H atoms were omitted for clarity.

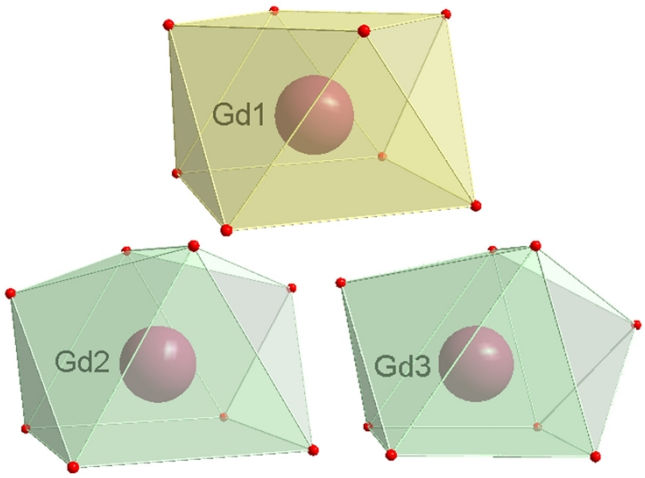

Fig. S5 Coordination polyhedra for **Gd_{14}**.

Table S4 Continuous Shape Measures (CShMs) of the coordination geometry for Gd^{III} ion in **Gd_{14}**. (CShMs values calculated with the Shape program). The CShMs values indicated the proximity to the ideal polyhedron, thus, CShMs = 0 corresponds to the non-distorted polyhedron. The three closer ideal geometries to the real complexes are listed and below are the symmetry and description for each polyhedron.

	CShMs	Polyhedron
Gd1	**0.699**	**SAPR-8 D_{4d} Square antiprism**
	1.604	BTPR-8 C_{2v} Biaugmented trigonal prism
	3.111	JBTPR-8 C_{2v} Biaugmented trigonal prism J50
Gd2	**0.102**	**BTPR-8 C_{2v} Biaugmented trigonal prism**
	1.776	JBTPR-8 C_{2v} Biaugmented trigonal prism J50

	2.358	SAPR-8 D_{4d} Square antiprism
Gd3	**1.138**	**BTPR-8 C_{2v} Biaugmented trigonal prism**
	1.903	JBTPR-8 C_{2v} Biaugmented trigonal prism J50
	3.195	TDD-8 D_{2d} Triangular dodecahedron

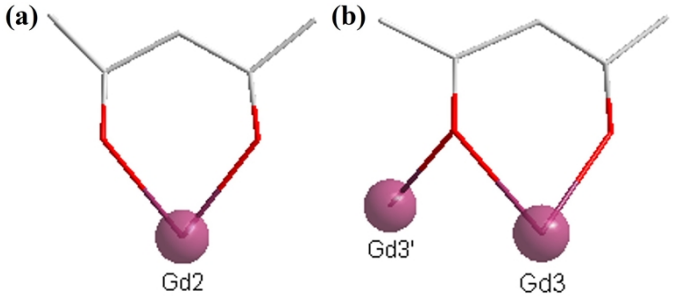

Fig. S6 Coordination patterns of ligand in **Gd_{14}**. Color code: Gd (plum), O (red), C (grey). H atoms were omitted for clarity.

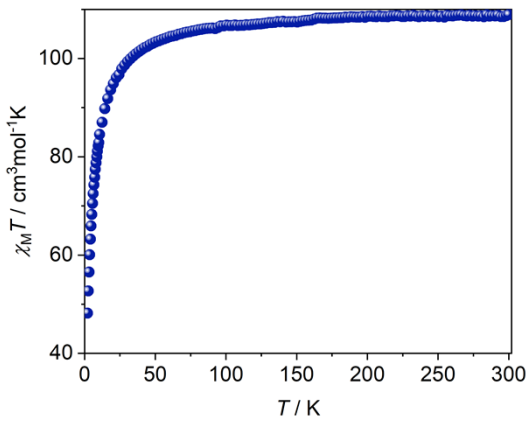

Fig. S7 Plot of experimental magnetic susceptibility ($\chi_M T$) versus T for **Gd_{14}**.

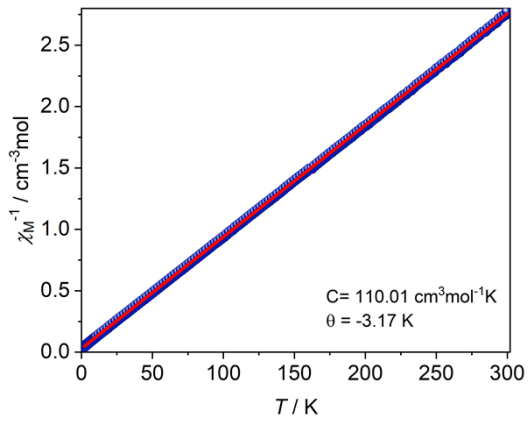

Fig. S8 χ_M^{-1} versus T plot of **Gd_{14}**. The red line is the fitting result with $\chi_M = C / (T - \vartheta)$.

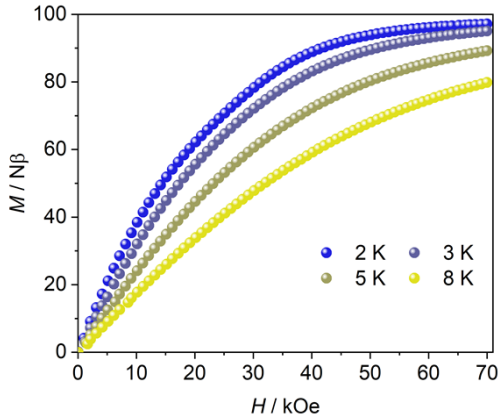

Fig. S9 Field dependences of magnetization in the field range 0-70 kOe for **Gd_{14}** at 2, 3, 5 and 8 K.

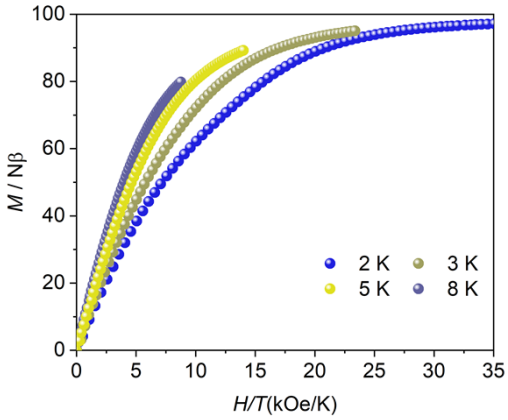

Fig. S10 Magnetization *M* vs *H*/*T* curves of **Gd_{14}** at 2, 3, 5 and 8 K.

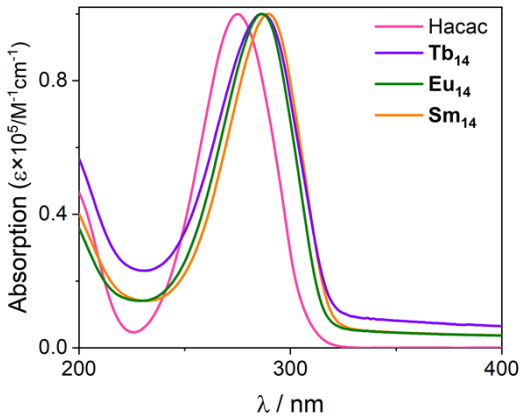

Fig. S11 UV-vis absorption spectra of the ligand and complexes.

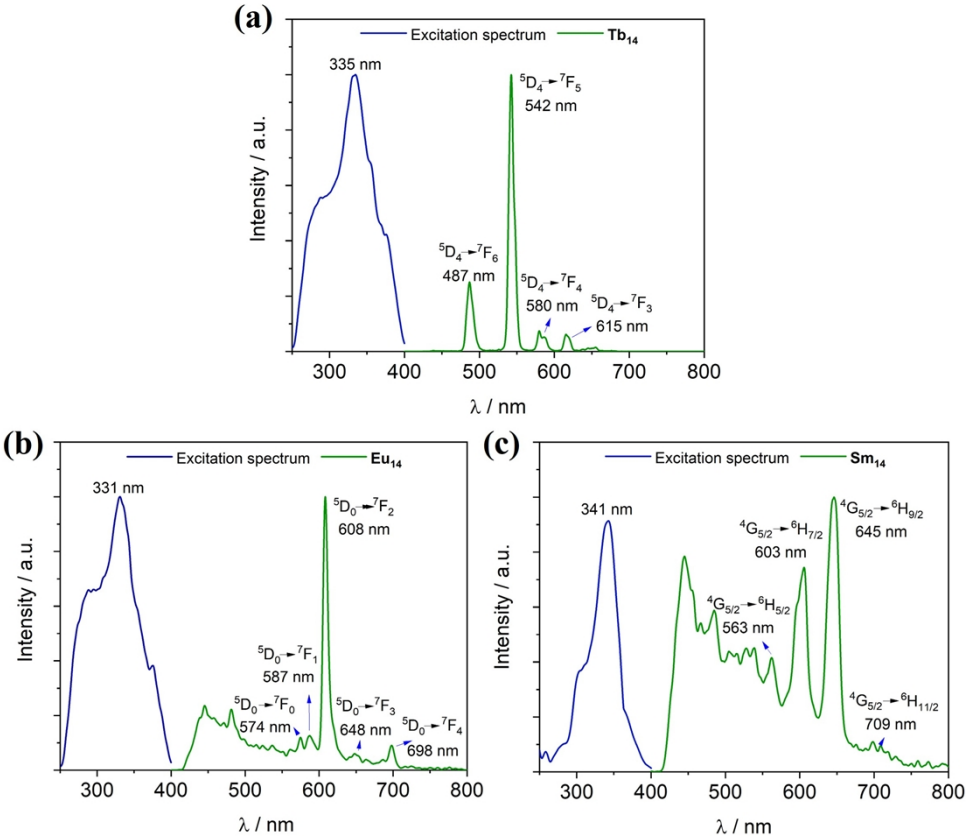

Fig. S12 Excitation and emission spectra of the complexes.

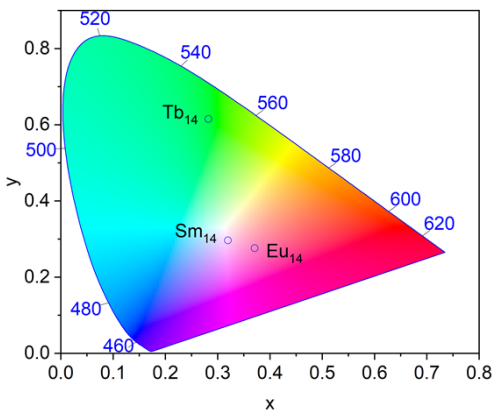

Fig. S13 CIE coordinates of **Ln_{14}**.

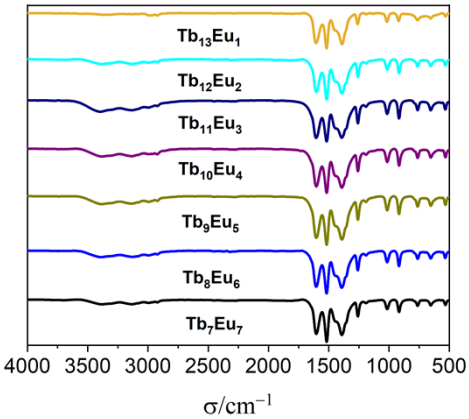

Fig. S14 Infrared spectra of **Tb_xEu_{14-x}**.

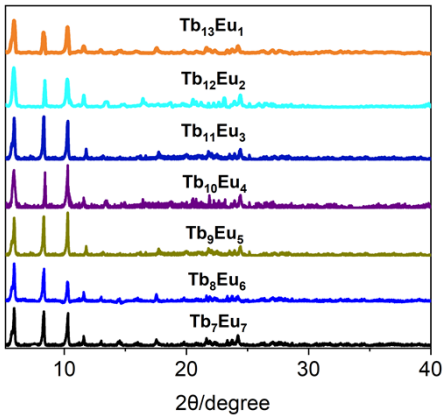

Fig. S15 Experimental PXRD patterns of **Tb_xEu_{14-x}**.

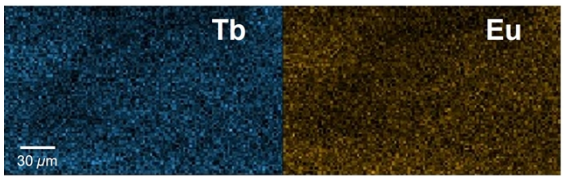

Fig. S16 The EDX mapping of **Tb_9Eu_5**.

Table S5 ICP results of the heterometallic clusters. Calculated and experimental values.

Cluster	Tb^{III}/%		Eu^{III}/%	
	calculated	experimental	calculated	experimental
$Tb_{13}Eu_1$	92.86	92.73	7.14	7.27
$Tb_{12}Eu_2$	85.71	85.89	14.29	14.11
$Tb_{11}Eu_3$	78.57	78.72	21.43	21.28
$Tb_{10}Eu_4$	71.43	71.51	28.57	28.49
Tb_9Eu_5	64.29	64.17	35.71	35.83
Tb_8Eu_6	57.14	57.03	42.86	42.97
Tb_7Eu_7	50.00	50.18	50.00	49.82

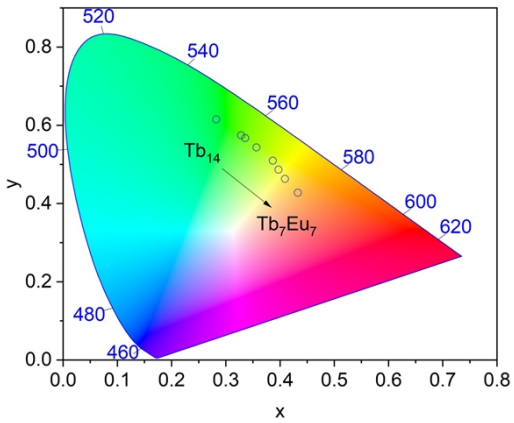

Fig. S17 CIE coordinates of Tb_xEu_{14-x}.

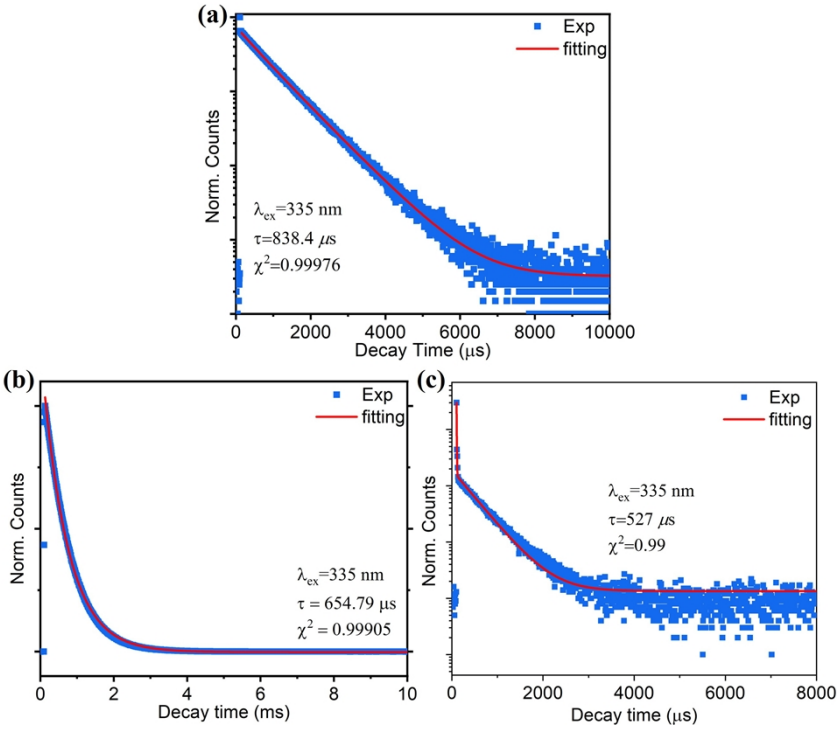

Fig. S18 (a) **Tb_{14}**, (b) **Tb_9Eu_5** and (c) **Tb_9Eu_5** after OFX detection fluorescence lifetimes of $^5D_4$ monitoring emission peaks at 542 nm.

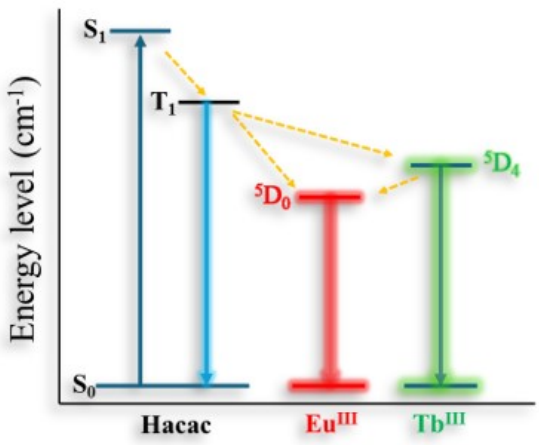

Fig. S19 Energy level diagram of the Tb_xEu_{14-x}.

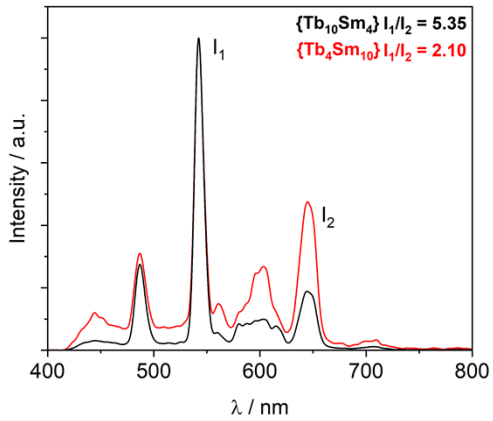

Fig. S20 Emission spectra (λ_{ex} = 335 nm) for $\mathbf{Tb_{10}Sm_4}$ (black line) and $\mathbf{Tb_4Sm_{10}}$ (red line).

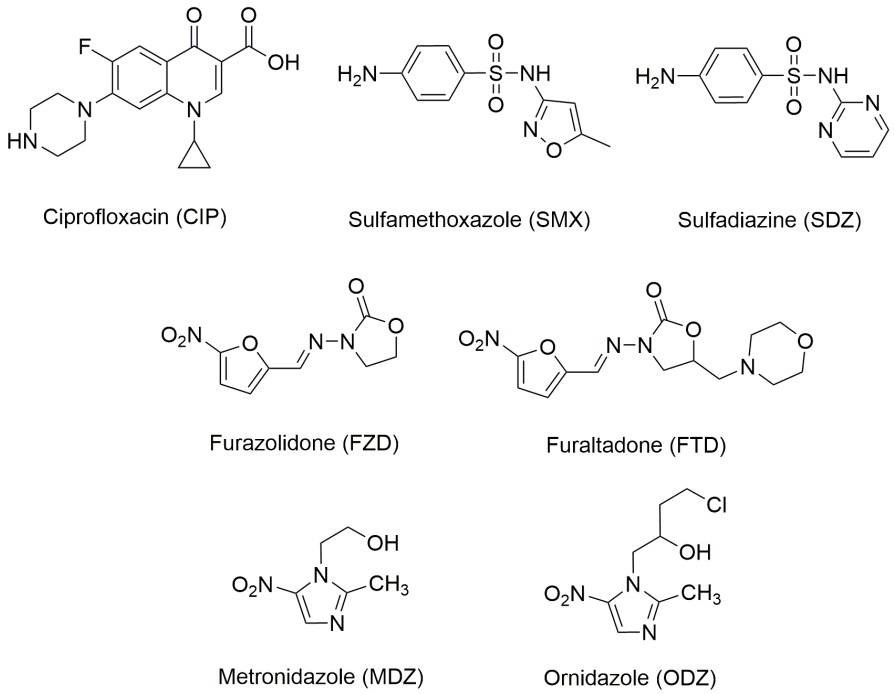

Scheme S1 Chemical structures of antibiotics.

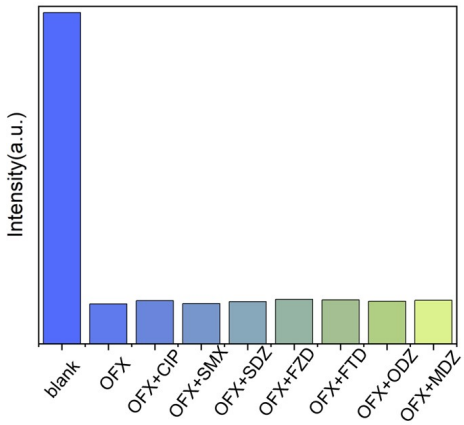

Fig. S21 Relative emission intensity of **Tb_{14}** in diverse antibiotic solutions with OFX (λ_{ex} = 335 nm).

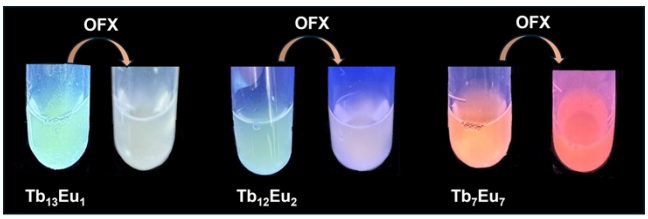

Fig. S22 Color changes of **$Tb_{13}Eu_1$**, **$Tb_{12}Eu_2$**, and **Tb_7Eu_7** solutions upon addition of 100 μM OFX under UV light.

Table S6 Changes in the I_{608nm}/I_{542nm} ratio of **Tb_8Eu_6**, **Tb_9Eu_5**, **$Tb_{10}Eu_4$**, and **$Tb_{11}Eu_3$** before and after the addition of 100 μM OFX.

	I_{608nm}/I_{542nm} (0 μM OFX)	I_{608nm}/I_{542nm} (100 μM OFX)	Relative Change
Tb_8Eu_6	1.12	2.59	131%
Tb_9Eu_5	0.85	2.34	175%
$Tb_{10}Eu_4$	0.60	1.48	147%
$Tb_{11}Eu_3$	0.42	1.12	166%

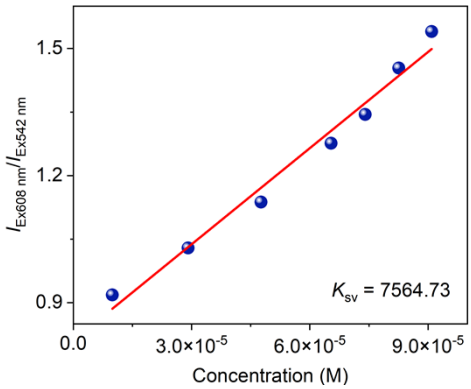

Fig. S23 Linear relationship between fluorescence intensity ratio (I_{608}nm/I_{542}nm) and OFX concentration.

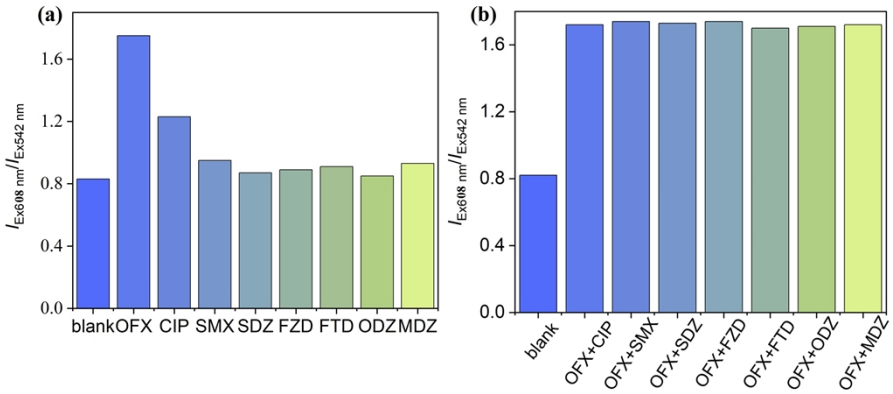

Fig. S24 Relative emission intensity of **Tb_9Eu_5** in diverse antibiotic solutions with and without OFX (λ_{ex} = 335 nm).

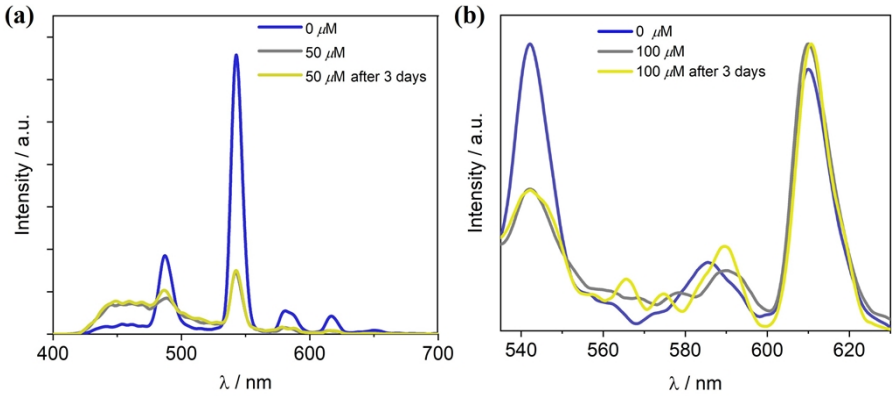

Fig. S25 The emission spectra of **Tb_{14}** (a) and **Tb_9Eu_5** (b) with the addition of OFX.

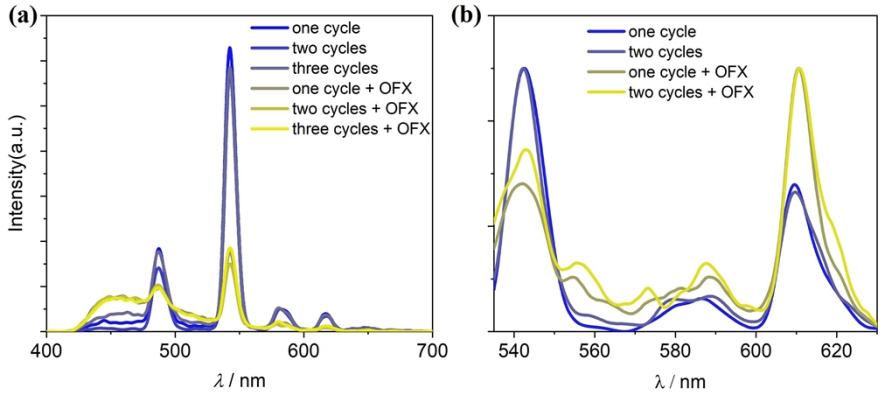

Fig. S26 The luminescence response of **Tb_{14}** (a) and **Tb_9Eu_5** (b) after 2-3 times recycled with the addition of 50/100 μM of OFX. (λ_{ex} = 335 nm).

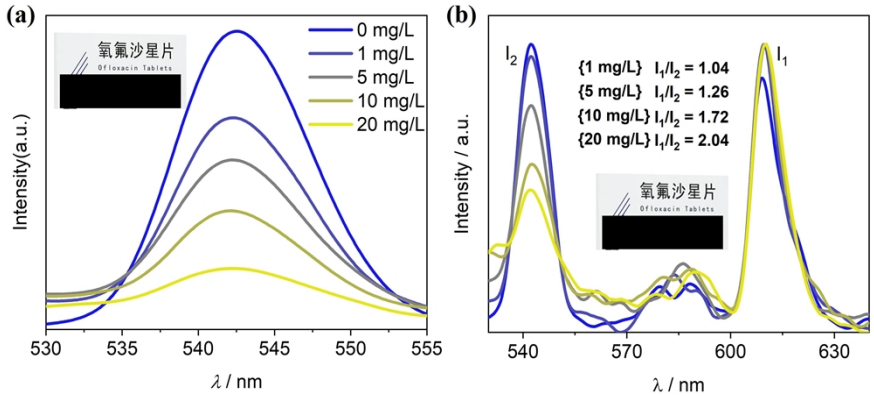

Fig. S27 The luminescence response of **Tb_{14}** (a) and **Tb_9Eu_5** (b) to the antibiotic drug Ofloxacin (including OFX). Inset: a photo of the drug ofloxacin sold in a pharmacy.

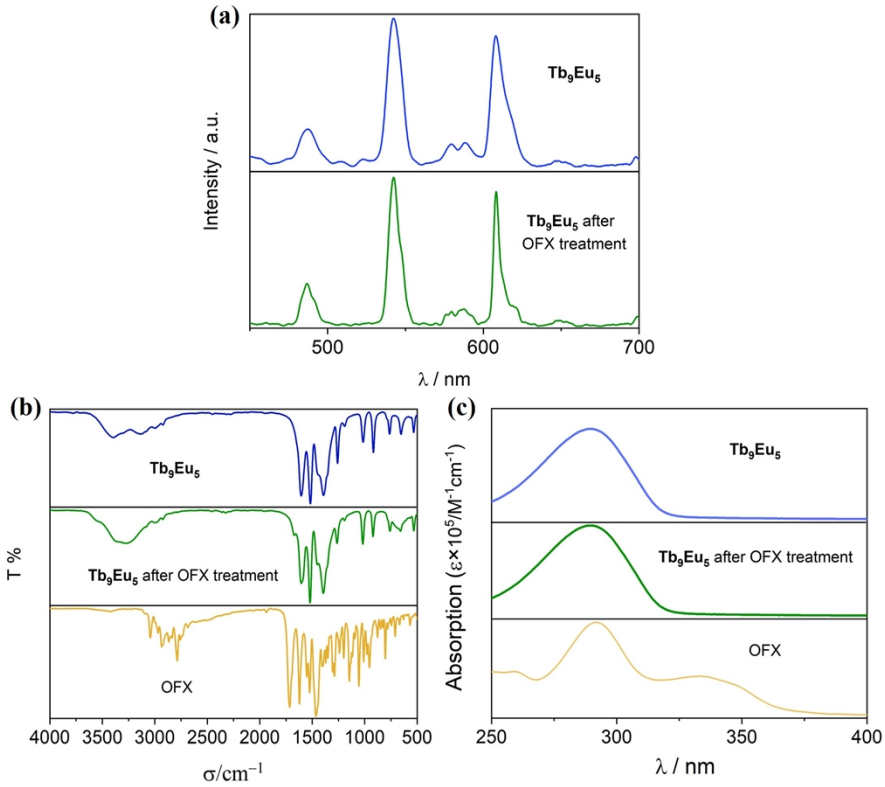

Fig. S28 Luminescence spectrum (a), Infrared spectrum (b) and UV–Vis absorption spectrum (c) of **Tb_9Eu_5** before and after OFX treatment.

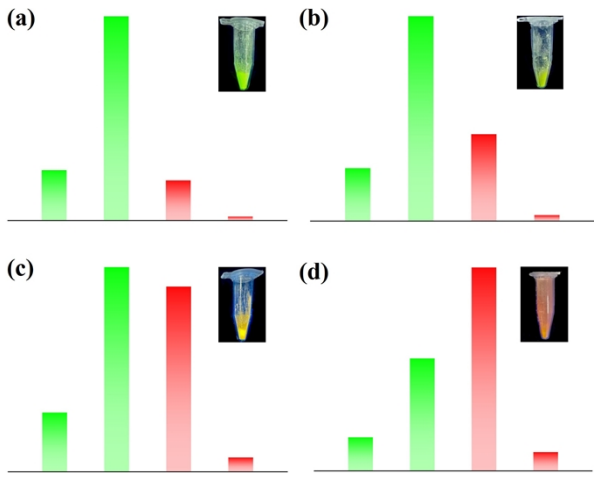

Fig. S29 Color-coded schematic of the barcode readout a) {**$Tb_{13}Eu_1$**}, b) {**$Tb_{11}Eu_3$**}, c) {**Tb_9Eu_5**} and d) {**Tb_7Eu_7**}. From left to right, the bars refer to the follow transitions: $^5D_4 \rightarrow {}^7F_6$ (487 nm), $^5D_4 \rightarrow {}^7F_5$ (542 nm), $^5D_0 \rightarrow {}^7F_2$ (608 nm), and $^5D_0 \rightarrow {}^7F_4$ (698 nm). Green and red bars refer to Tb^{III} and Eu^{III} emissions, respectively.

The analysis of frontier molecular orbitals

The crystal structure of **Tb_{14}** was evaluated using Gaussian16. Single-point energy calculations were performed at the PBE0/6-31G** level for C, H, and O atoms, and at the PBE0/MWB54 level for Tb. All atoms in the interfering species were also subjected to single-point energy calculations at the PBE0/6-31G** level. Dispersion corrections were applied using Becke-Johnson (BJ) damping (keyword: em=gd3bj).[1]

References

1. M. J. Frisch, G. W. Trucks, H. B. Schlegel, G. E. Scuseria, M. A. Robb, J. R. Cheeseman, G. Scalmani, V. Barone, G. A. Petersson, H. Nakatsuji, X. Li, M. Caricato, A. V. Marenich, J. Bloino, B. G. Janesko, R. Gomperts, B. Mennucci, H. P. Hratchian, J. V. Ortiz, A. F. Izmaylov, J. L. Sonnenberg, D. Williams-Young, F. Ding, F. Lipparini, F. Egidi, J. Goings, B. Peng, A. Petrone, T. Henderson, D. Ranasinghe, V. G. Zakrzewski, J. Gao, N. Rega, G. Zheng, W. Liang, M. Hada, M. Ehara, K. Toyota, R. Fukuda, J. Hasegawa, M. Ishida, T. Nakajima, Y. Honda, O. Kitao, H. Nakai, T. Vreven, K. Throssell, J. A. Montgomery Jr., J. E. Peralta, F. Ogliaro, M. J. Bearpark, J. J. Heyd, E. N. Brothers, K. N. Kudin, V. N. Staroverov, T. A. Keith, R. Kobayashi, J. Normand, K. Raghavachari, A. P. Rendell, J. C. Burant, S. S. Iyengar, J. Tomasi, M. Cossi, J. M. Millam, M. Klene, C. Adamo, R. Cammi, J. W. Ochterski, R. L. Martin, K. Morokuma, O. Farkas, J. B. Foresman and D. J. Fox, *Journal*, 2016.